![ACS OMEGA]

Article

Rational Design of W-Doped Ag₃PO₄ as an Efficient Antibacterial Agent and Photocatalyst for Organic Pollutant Degradation

Aline B. Trench,* Thales R. Machado,* Amanda F. Gouveia, Camila C. Foggi, Vinícius Teodoro, Isaac Sánchez-Montes, Mayara M. Teixeira, Letícia G. da Trindade, Natalia Jacomaci, Andre Perrin, Christiane Perrin, Jose M. Aquino, Juan Andrés, and Elson Longo*

Read Online

ACCESS | Metrics & More | Article Recommendations | Supporting Information

ABSTRACT: Bacterial and organic pollutants are major problems with potential adverse impacts on human health and the environment. A promising strategy to alleviate these impacts consists in designing innovative photocatalysts with a wider spectrum of application. In this paper, we report the improved photocatalytic and antibacterial activities of chemically precipitated Ag_3PO_4 microcrystals by the incorporation of W at doping levels 0.5, 1, and 2 mol %. The presence of W directly influences the crystallization of Ag_3PO_4, affecting the morphology, particle size, and surface area of the microcrystals. Also, the characterization via experimental and theoretical approaches evidenced a high density of disordered $[AgO_4]$, $[PO_4]$, and $[WO_4]$ structural clusters due to the substitution of P^{5+} by W^{6+} into the Ag_3PO_4 lattice. This leads to new defect-related energy states, which decreases the band gap energy of the materials (from 2.27 to 2.04 eV) and delays the recombination of $e'-h^\bullet$ pairs, leading to an enhanced degradation process. As a result of such behaviors, W-doped Ag_3PO_4 (Ag_3PO_4:W) is a better visible-light photocatalyst than Ag_3PO_4, demonstrated here by the photodegradation of potential environmental pollutants. The degradation of rhodamine B dye was 100% in 4 min for Ag_3PO_4:W 1%, and for Ag_3PO_4, the obtained result was 90% of degradation in 15 min of reaction. Ag_3PO_4:W 1% allowed the total degradation of cephalexin antibiotic in only 4 min, whereas pure Ag_3PO_4 took 20 min to achieve the same result. For the degradation of imidacloprid insecticide, Ag_3PO_4:W 1% allowed 90% of degradation, whereas Ag_3PO_4 allowed 40%, both in 20 min of reaction. Moreover, the presence of W-dopant results in a 16-fold improvement of bactericidal performance against methicillin-resistant *Staphylococcus aureus*. The outstanding results using the Ag_3PO_4:W material demonstrated its potential multifunctionality for the control of organic pollutants and bacteria in environmental applications.
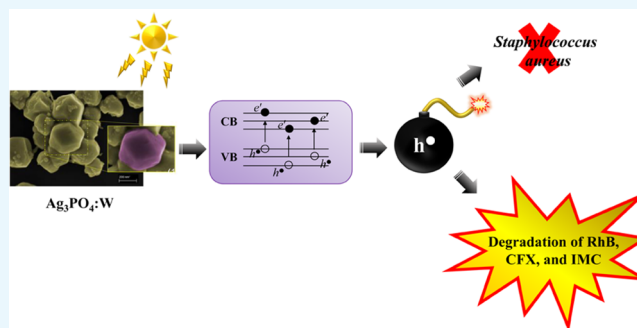
INTRODUCTION

In the past years, great efforts have been devoted to the search and development of new environmentally friendly photocatalysts for the control of pollutants and water purification as a way to solve great problems associated with the increasing pollution at the surface of the Earth.[1,2] Since Fujishima and Honda demonstrated in 1972 that titanium dioxide (TiO_2) could be used as a photoanode to split water excited by ultraviolet light, TiO_2-based catalysts appeared as the most promising approach to solve the global energy crisis and environmental problems due to their low cost and high stability.[3,4] However, the development of such materials is limited because TiO_2 can only be activated under ultraviolet light, which is a small fraction (around 5%) of solar light, making it more difficult to harvest the remaining solar energy[5,6] and obtain a fast recombination rate of photoinduced electron−hole ($e'-h^\bullet$) pairs.

The limitation of the visible-light harvesting capacity of TiO_2 has motivated researchers to design new single-phase photo-catalyst materials with superior visible-light photoactivity.[7] Silver orthophosphate (Ag_3PO_4), a traditional Ag-based semiconductor, is a potential candidate because of its appropriate band gap energy (2.36 eV), nontoxicity, and high photocatalytic activity for the degradation of organic pollutants under visible-light irradiation. The delocalized π^* antibonding states formed on the conduction band (CB) can facilitate the separation of charge carriers. Moreover, the inductive effect of PO_4^{3-} anions further promotes the separation of charge carriers.[8] Although Ag_3PO_4 has been found to exhibit a higher photocatalytic activity in the degradation of organic dyes than TiO_2,[9−12] this material can

also be considered a promising antibacterial agent for environmental remediation.[13−16] Further technological breakthroughs have been presented combining Ag_3PO_4 and ceftazidime for sterilization and residue removal[17] as well as Ag_3PO_4 and lidocaine to prevent infections.[18] However, the practical application of Ag_3PO_4 is restricted by the photocorrosion resulting from its poor photostability and rapid recombination of photogenerated $e'−h^\bullet$ pairs.[19,20]

Consequently, it was necessary to overcome those drawbacks by developing modified Ag_3PO_4 materials to obtain optimized photocatalytic activity and stability.[21] As recently discussed and summarized by Li et al.,[22] the progress in the field includes the control of the Ag_3PO_4 exposed facets, incorporation of dopants in the Ag_3PO_4 crystalline lattice, coupling Ag_3PO_4 with metal nanoparticles, and the construction of heterostructured composites. In particular, the use of cations (Bi^{3+}, Ba^{2+}, Ni^{2+}, and Mn^{2+})[23−26] and anions ($SO_4^{2−}$ and $CO_3^{2−}$)[27,28] as dopants may not only retard charge pair recombination but also enable enhanced visible-light absorption by providing defect states in the band-gap region to improve the photocatalytic activity.[29]

Our group was strongly involved in the theoretical and experimental studies on the structural, optical, and photocatalytic properties of pure and doped Ag_3PO_4.[30−32] Very recently, we reported a new Mo-doped silver orthophosphate (Ag_3PO_4:Mo) material with enhanced photocatalytic activity.[33] This work points out that Mo acts as a dopant, provoking the appearance of defects in the Ag_3PO_4 structure, which significantly improves its photocatalytic performance (100% rhodamine B (RhB) degradation within 5 min). The results were reinforced by the findings of Hussien et al.,[34] who observed 98% of methylene blue degradation within 5 min. Considering previous successful research studies, our present aim was to obtain W-doped Ag_3PO_4 (Ag_3PO_4:W) for wider environmental applications. Until now, little is known about this doping process or its consequences on Ag_3PO_4 final properties and only Ag_3PO_4/WO_3 composites were prepared.[35−37] In this sense, it is expected that the the W^{6+} dopant replaces P^{5+} cations in the Ag_3PO_4 lattice, possibly generating different types of structural and electronic defects and modifying the intermediate energy levels in the band-gap region, which are essential to improve the performance of Ag_3PO_4.

Based on the above considerations, a detailed experimental work via structural, morphological, and compositional characterizations of Ag_3PO_4:W microcrystals was performed. The obtained data was complemented by first-principles calculations. The degradation of organic pollutants including RhB, the antibiotic cephalexin (CFX), and the insecticide imidacloprid (IMC) by Ag_3PO_4:W samples was investigated. We also studied the antibacterial activity of the materials by testing them against methicillin-resistant *Staphylococcus aureus* (MRSA).

■ RESULTS AND DISCUSSION

X-ray Diffraction (XRD) and Rietveld Refinement. First crystallographic studies showed that Ag_3PO_4 crystallizes in a cubic structure ($P\bar{4}3n$ space group) based on a body-centered cubic stacking of an isolated regular $[PO_4]$ tetrahedral cluster with P−O bond distances of 1.548 Å. Each Ag^+ cation is located at a fully occupied oxygen site of −4 symmetry.[38,39] Further refinements showed that the position of the Ag^+ cation was in fact split from the 12h site of 2-fold symmetry with half

occupancy.[40,41] Consequently, the $[AgO_4]$ tetrahedral cluster was distorted with two different Ag−O distances, 2.357 Å × 2 and 2.404 Å × 2.[42]

Powder XRD patterns of pure Ag_3PO_4 and Ag_3PO_4:W (0.5−2%) are displayed in Figure 1, and their respective Rietveld

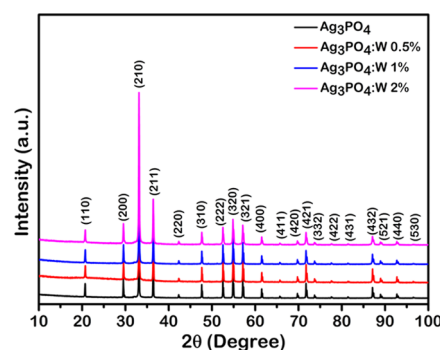**Figure 1.** XRD patterns of Ag_3PO_4, Ag_3PO_4:W 0.5%, Ag_3PO_4:W 1%, and Ag_3PO_4:W 2% samples.

refinements are illustrated in Figure S1. The patterns are clearly in full agreement with the data relative to Ag_3PO_4 with a cubic structure, as reported in the Inorganic Crystal Structure Database (ICSD) no. 14000[39] and no. 1530.[40] No impurities such as α-Ag_2WO_4 were found in the samples. This contrasts with our previous results obtained for the doping of Ag_3PO_4 with Mo,[33] in which a well-crystallized secondary phase related to the presence of β-Ag_2MoO_4 was clearly detected above the limit of 2% Mo doping level. No diffraction peaks of expected structural phases related to W were observed, indicating the incorporation of the W cation into the Ag_3PO_4 structure as a doping element.

Table S1 gathers the crystal data from Rietveld refinements for our samples of pure Ag_3PO_4 and Ag_3PO_4:W with 0.5, 1, and 2% W. It can be seen that the lattice constant and volume slightly increase from 0 to 1%, while an opposite behavior occurs when the W concentration increases to 2%. The overall difference in lattice constants and volume is almost negligible. Under such conditions, it is not possible to accurately determine the doping limit by simply examining the XRD powder patterns.

From the results of Rietveld refinements for the pure Ag_3PO_4 sample, we constructed theoretical models, as illustrated in Figure 2a,b. The optimized calculations lead to a structure for pure Ag_3PO_4 (Figure 2a) composed of $[PO_4]$ and $[AgO_4]$ clusters, with $[PO_4]$ clusters forming a tetrahedral arrangement with equal P−O bond length (1.5642 Å) and O−P−O angles (109.47°) and $[AgO_4]$ clusters presenting two values of O−Ag−O angles (149.87 and 93.87°) with equal Ag−O bond length (2.4306 Å). The result concerning the length of Ag−O bonds goes against that observed in the literature, where two different bond distances were found.[42] This is because the theoretical optimized structure is ideal and perfect in vacuum, without the presence of defects.

The W doping into the Ag_3PO_4 structure induced structural distortions in the crystal lattice and coordination parameters of clusters, as shown in Figure 2b, which can be seen as changes in bond lengths and angles of the $[PO_4]$ and $[AgO_4]$ clusters. Specifically, the W doping process had been shown to induce different average bond lengths for all of the clusters composing the Ag_3PO_4 structure. It was also possible to observe larger P−O and Ag−O bond lengths in the $[PO_4]$ and $[AgO_4]$ clusters,
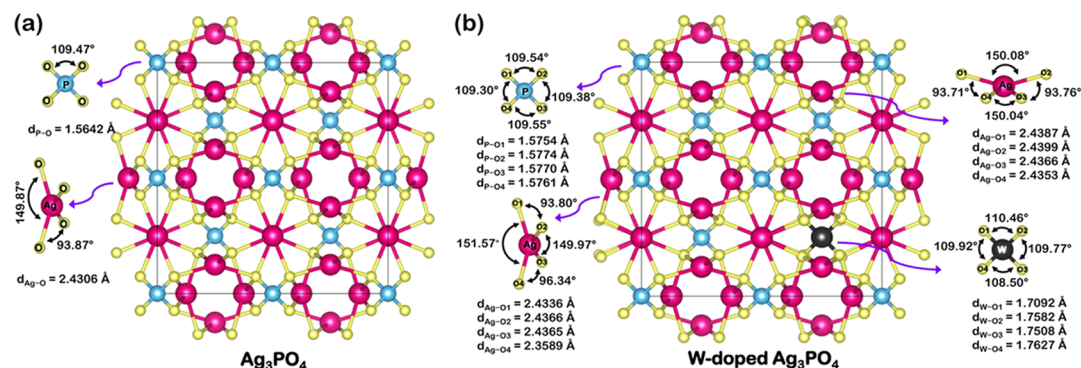
Figure 2. Schematic representation of the $2 \times 2 \times 2$ supercell periodic models built for (a) pure Ag_3PO_4 and (b) Ag_3PO_4:W.

respectively, compared to the pure sample. The resulting cluster of the doping process, the tetrahedral $[WO_4]$ cluster, also presented a distorted nature (distinct average bond lengths and angles) and possessed a longer bond length than the $[PO_4]$ cluster of the pure sample. These behaviors lead to a range of average values and an increase in the local structure disorder, which can profoundly affect the final properties of the studied materials.

Micro-Raman Spectroscopy. Figure 3a shows the Raman spectra obtained for pure Ag_3PO_4 and Ag_3PO_4:W 0.5, 1, and

Figure 3. (a) Raman spectra and (b) A_1 Raman mode of Ag_3PO_4, Ag_3PO_4:W 0.5%, Ag_3PO_4:W 1%, and Ag_3PO_4:W 2%.

2% samples. The spectrum of the pure Ag_3PO_4 is in good agreement with the data previously reported by our research group.[31,33] Eighteen Raman-active modes were expected, but only a few of them were experimentally observed due to an overlapping and/or weak relative intensity. The 1000 cm^{-1} (weak) and 911 cm^{-1} (strong) bands are attributed to T_2 asymmetric and A_1 symmetric stretching modes of the $[PO_4]$ tetrahedron, respectively. A weak scattering band was observed near 701 cm^{-1}, related to a symmetric stretching of the $[PO_4]$

tetrahedron. Based on our previous results, it is not assigned to any first-order normal mode of the Ag_3PO_4 structure and thus could originate from a combination mode, implying the 250 and 458 cm^{-1} wave numbers (for T_2 and A_1, respectively), for instance, in their calculated spectrum. The T_2 band observed at approximately 549 cm^{-1} is attributed to the bending mode of the $[PO_4]$ tetrahedron, as well the expected modes located at approximately 400 (E) and 220 cm^{-1} (T_2), the last two being not observable due to their weak intensity. The band near 100 cm^{-1} can be associated with translation and/or rotational modes of the T_2 symmetry. All observed Raman bands for all samples are related to Ag_3PO_4 with no secondary phase, indicating the effectiveness of W doping into the Ag_3PO_4 structure.

As it can be seen in Figure 3a, the samples of pure Ag_3PO_4 and Ag_3PO_4:W doped up to 1% presented Raman scattering bands, whereas an increase of W dopant to 2% led to an absence of almost all observed modes for Ag_3PO_4, including the most intense one (A_1) at approximately 911 cm^{-1}. The only observed mode for this sample can be related to translational and/or rotational modes of the structure, while the vibrational modes linked to $[PO_4]$ clusters were absent in the observed spectrum. This band absence is associated with a relative excessive amount of dopant, i.e., the solubility limit of the W dopant in the Ag_3PO_4 structure, which causes a symmetry breaking of the local structure as a result of the high structural disorder density in the composing clusters. This symmetry breaking provokes a break of degrees of freedom, resulting in the absence of $[PO_4]$ clusters subjected to Raman scattering. The point of solubility limit was not observed in XRD patterns due to some technique conditions that were able to detect the structural order at a long range, i.e., the unit cell periodicity. The phase transformation of a dopant into a secondary phase initiates from a short-range structural ordering, which includes bond breaking for later structural rearrangement of the composing clusters. The point of structural changes for a possible rearrangement in the secondary phase was observed for the Ag_3PO_4:W 2% sample. Therefore, as the main goal of this work was to study the W doping effects on the structural, optical, photocatalytic, and antibacterial properties of Ag_3PO_4, all of the other characterization techniques were only employed for pure Ag_3PO_4 and Ag_3PO_4:W 0.5 and 1% samples, since the solubility limit was reached in the Ag_3PO_4:W 2% sample.

It can be observed in Figure 3a that the increase of W-dopant concentration caused an increase in the T_2 band intensity located at approximately 1000 cm^{-1}, besides the emergence of two other bands located at approximately 549
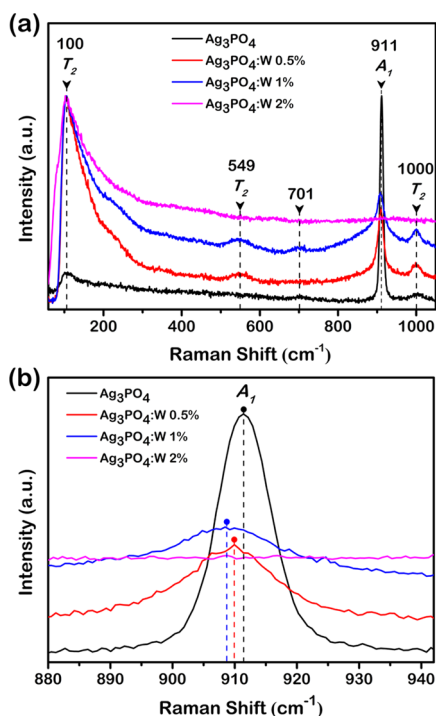
cm^{-1} (T_2) and 701 cm^{-1}, which were not observed for the pure Ag$_3$PO$_4$ sample. The introduction of W dopant into the crystal lattice provokes local structural changes due to its difference in electron density in comparison with the host P ions in [PO$_4$] clusters. This difference leads to changes in bond angles and lengths of the W-modified cluster and structural changes in the adjacent clusters (Figure 2b). These structural variations cause a polarization of the clusters, capable of affecting their electron densities. The Raman scattering arises from polarizability of the structure that allows the light scattering; hence, the higher the polarizability, the higher the Raman scattering. A similar behavior was previously reported for Mo-doped Ag$_3$PO$_4$ samples, which was considered as the signature of a local disorder.[33] Therefore, the W doping into the Ag$_3$PO$_4$ lattice leads to structural distortions that induce cluster polarization, resulting in a higher polarizability and consequently the appearance of two Raman bands.

A remarkable broadening of the most intense Raman band (A_1 mode, at approximately 911 cm^{-1}) was observed with the increase in the W doping concentration compared to pure Ag$_3$PO$_4$. As already mentioned in the XRD section, the theoretical calculations indicated that the incorporation of W into the Ag$_3$PO$_4$ structure induces four different average bond lengths for the [PO$_4$] cluster, in contrast to the pure Ag$_3$PO$_4$, which presented only one bond length for the same cluster. Since the A_1 Raman mode observed in the spectra is related to the symmetric stretching of O−P−O bonds, its average bond length directly influences the frequency of the vibrational mode and consequently the Raman shift value. For a given vibrational mode, there is a specific range of frequency allowed for the structure. Therefore, the greater the range of frequencies of a vibrational mode, the greater the bandwidth of the respective Raman shift band due to several allowed frequencies scattering the incident light. Therefore, the observed broadening of the most intense Raman shift band as a function of W doping concentration corroborates the theoretical calculation results, since the W doping provokes a range of bond lengths for [PO$_4$] clusters.

Furthermore, a shift in the value of the A_1 Raman band was observed with an increase in the W doping concentration compared to pure Ag$_3$PO$_4$. As can be seen in Figure 3b, such an increase led to a displacement of the Raman band to lower frequency values, which were 911.4, 909.9, and 908.7 cm^{-1} for pure Ag$_3$PO$_4$, Ag$_3$PO$_4$:W 0.5%, and Ag$_3$PO$_4$:W 1% samples, respectively. Hereupon, the displacements were 1.5 cm^{-1} from pure Ag$_3$PO$_4$ to 0.5%W and 1.2 cm^{-1} from the latter to 1%W samples. Based on Badger's rule improved by Herschbach and Laurie, the bond length and vibrational frequency of a stretching mode has an inversely linear correlation, i.e., the longer the bond length, the lower the vibrational frequency.[43−45] These results were clearly observed in the experimental Raman spectra of the samples, indicating the introduction of W as a substitutional dopant in the Ag$_3$PO$_4$ structure. According to our theoretical calculations previously described in the XRD section, the introduction of W into the Ag$_3$PO$_4$ structure resulted in longer bond lengths of [PO$_4$] clusters, which corroborates the observed displacement of the A_1 Raman band to lower frequencies. Therefore, these experimental observations and the theoretical calculations support the introduction of W into Ag$_3$PO$_4$ as a substitutional dopant.

X-ray Photoelectron Spectroscopy (XPS) Analysis. This technique was used to identify the surface composition

and valence states present in the Ag$_3$PO$_4$, Ag$_3$PO$_4$:W 0.5 and 1% samples. The survey spectra shown in Figure 4a indicated

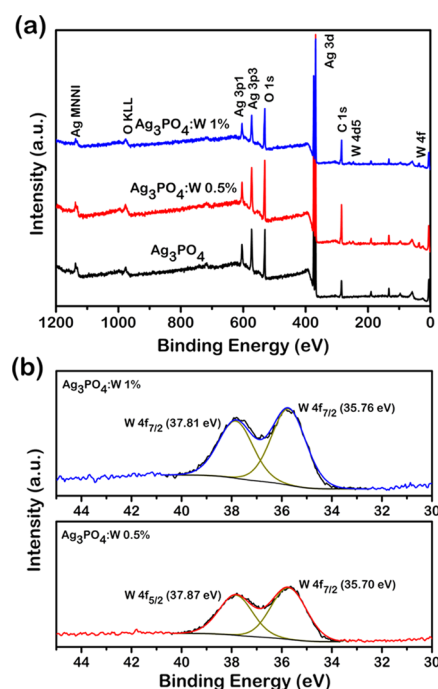**Figure 4.** (a) XPS spectra of Ag$_3$PO$_4$, Ag$_3$PO$_4$:W 0.5%, and Ag$_3$PO$_4$:W 1% samples and (b) W 4f high-resolution spectra of Ag$_3$PO$_4$:W 0.5% and Ag$_3$PO$_4$:W 1%.

the presence of sole main peaks associated with the elements Ag, P, W, O, and C (adsorbed and/or from the XPS instrument). The elemental surface quantification (Table 1)

Table 1. Elemental Surface Quantification by XPS of the Distinct Samples

sample	Ag (atom %)	P (atom %)	W (atom %)	O (atom %)	Ag/P
Ag$_3$PO$_4$	30.25	20.63		49.12	1.5
Ag$_3$PO$_4$:W 0.5%	29.84	16.58	1.21	52.36	1.7
Ag$_3$PO$_4$:W 1.0%	29.30	14.20	1.67	54.83	2.0

confirms the presence of W in both Ag$_3$PO$_4$:W 0.5 and 1% samples at the doping levels. The Ag/P atomic ratio gradually increases with the introduction of W, which can be related to the substitution process of P^{5+} by W^{6+}. Moreover, the samples presented a Ag/P ratio lower than the expected value of 3 for the Ag$_3$PO$_4$ structure. Since no secondary phases were identified in all of these samples, this could imply distinct composition comparing the bulk and surface of the particles. Other adsorbed species such as water and CO$_2$ can also interfere in the quantitative results. A similar trend was observed in our recent publication regarding the Ag$_3$PO$_4$:Mo structure.[33]

Figure 4b shows the high-resolution XPS spectra of W in the 4f region of Ag$_3$PO$_4$:W 0.5 and 1% samples. Two main peaks at 37.8 and 35.7 eV can be observed, corresponding to the binding energies of W 4f$_{5/2}$ and W 4f$_{7/2}$ doublet, respectively, with a spin−orbit separation of 2.1 eV corresponding to the oxidation state W^{6+}.[46] Figure S2 shows the high-resolution XPS spectra of Ag in the 3d region for pure, Ag$_3$PO$_4$:W 0.5%, and Ag$_3$PO$_4$:W 1% samples. The peaks centered at ∼374 and
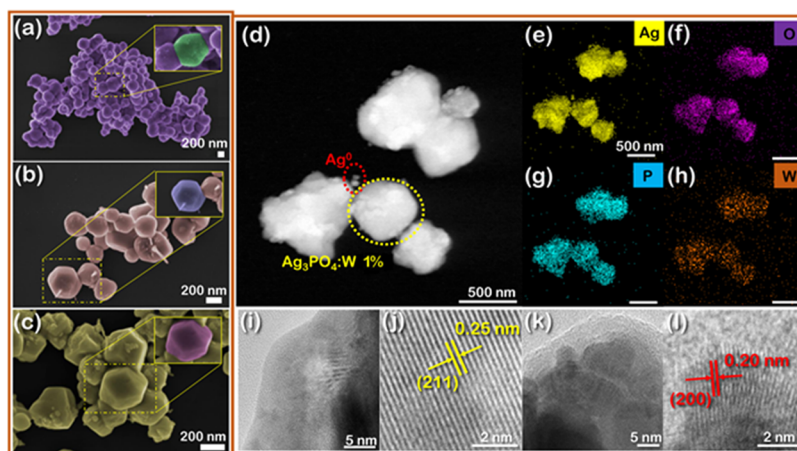
Figure 5. FESEM images of (a) Ag_3PO_4, (b) Ag_3PO_4:W 0.5%, and (c) Ag_3PO_4:W 1%. TEM images of the Ag_3PO_4:W 1% sample: (d) high-angle annular dark-field (HAADF) image showing two regions comprising Ag_3PO_4:W 1% and Ag^0 structures (yellow and red dotted circles, respectively), (e−h) EDS mapping of Ag, O, P, and W elements, (i, j) high-resolution TEM (HR-TEM) images of a border region of the Ag_3PO_4:W 1% crystal, and (k, l) HR-TEM images of Ag^0 nanostructures.

~368 eV are associated with Ag $3d_{3/2}$ and Ag $3d_{5/2}$ doublet, respectively.[47] Then, these peaks were further deconvoluted, revealing two components in each peak; those with the highest intensities centered at 373.9 and 367.9 eV correspond to Ag^+, while the other less intense peaks at 374.9 and 368.9 eV are attributed to the presence of Ag^0 in our samples.[48] The values calculated for the quantification of Ag^0 at the surface were 18.3, 20.7, and 19.6% for Ag_3PO_4, Ag_3PO_4:W 0.5%, and Ag_3PO_4:W 1%, respectively. The reduction of Ag^+ to Ag^0 can be related to an interaction between the sample and the XPS equipment, as in the case of transmission electron microscopy (TEM) characterization, since the samples are sensitive to the exposure to electromagnetic waves and electron beam.[33] The slightly higher values of Ag^0 in doped samples can be explained by the higher disorder in the Ag_3PO_4 structure induced by W^{6+}, which facilitates the reduction and extrusion processes. Figure S3 shows the high-resolution XPS spectra of O in the Ag_3PO_4 and Ag_3PO_4:W samples fitted in three components at 533.3, 531.9, and 530.5 eV. These components are related to adsorbed water molecules, surface hydroxyl groups, and lattice oxygen in the Ag_3PO_4 structure, respectively.[42,49] Figure S4 shows the high-resolution XPS spectra of P, where it is possible to observe two components at 134.2 and 132.8 eV attributable to P $2p_{1/2}$ and P $2p_{3/2}$ doublet, respectively, of P^{5+}.[49]

Field Emission Scanning Electron Microscopy (FESEM), TEM, and Brunauer−Emmett−Teller (BET) Analyses. The morphologies of Ag_3PO_4 samples are dependent on reagents, additives, procedure, pH, etc. used in the synthesis method.[21] Figure 5a−c displays the FESEM images of pure Ag_3PO_4, Ag_3PO_4:W 0.5%, and Ag_3PO_4:W 1%. The pure Ag_3PO_4 sample is composed of particles with an irregular spherical shape and an average diameter of 440 nm (Table 2 and Figure S5), which is in accordance with Ag_3PO_4 samples prepared under similar conditions.[50] The presence of W dopant affects mainly the shape (insets in Figure 5b,c) and size of the particles, and diameters in the range of 251 and 257 nm are observed for Ag_3PO_4:W 0.5 and 1% samples, respectively. Such behaviors were also observed for Mo-doped Ag_3PO_4[33] and can be related to the substitution process of P^{5+} by W^{6+}, which disturbs the crystallization process of the Ag_3PO_4 system. These results were corroborated with the data obtained by the adsorption−desorption isotherms at 77 K/

Table 2. Surface Area and Particle Size Values Obtained by BET and Particle Size Values Obtained by FESEM for the samples of Ag_3PO_4, Ag_3PO_4:W 0.5%, and Ag_3PO_4:W 1%

	FESEM	BET	
sample	particle size (nm)	particle size (nm)	surface area ($m^2\ g^{-1}$)
Ag_3PO_4	442	498	1.89
Ag_3PO_4:W 0.5%	251	207	4.52
Ag_3PO_4:W 1%	257	143	6.57

N_2 (Figure S6)—a gradual decrease in particle size and, as a consequence, an increase in specific surface area are observed as the W concentration increases (Table 2).

Figure 5d−l shows the TEM images of the Ag_3PO_4:W 1% sample. The HAADF image in Figure 5d indicates the presence of several particles with distinct sizes, corresponding to Ag_3PO_4:W 1% (yellow dotted circle) and Ag^0 (red dotted circle). To confirm this result, an elementary composition analysis of the sample was conducted by EDS mapping, and the results are exhibited in panels (e)−(h) in Figure 5. The sample presented a homogeneous distribution of Ag, P, W, and O elements, with no clear signs of W dopant segregation, corroborating with the incorporation of W in the Ag_3PO_4 structure. These results also confirm the formation of Ag^0 nanoparticles on the Ag_3PO_4 surface, which is induced by the electron beam of the TEM characterization, as recently demonstrated by our research group.[31] The crystalline features of our sample were analyzed by HR-TEM. Figure 5i shows an image of the border region of a single particle, and Figure 5j presents a magnified view of the corresponding lattice fringes. The interplanar distance at this spot was 0.25 nm, which can be indexed to the (211) plane of Ag_3PO_4 according to the ICSD database no. 14000. Figure 5k displays an HR-TEM image of some small nanoparticles formed on the Ag_3PO_4 surface, while Figure 5l brings a magnified view of these structures. The interplanar distance of 0.20 nm in this last figure can be indexed to the (200) plane of the cubic structure of Ag^0 according to the ICSD database no. 604630.

UV−Visible Diffuse Reflectance Spectroscopy and Electronic Properties. Figure 6a shows the UV−visible spectra of the Ag_3PO_4, Ag_3PO_4:W 0.5%, and Ag_3PO_4:W 1%
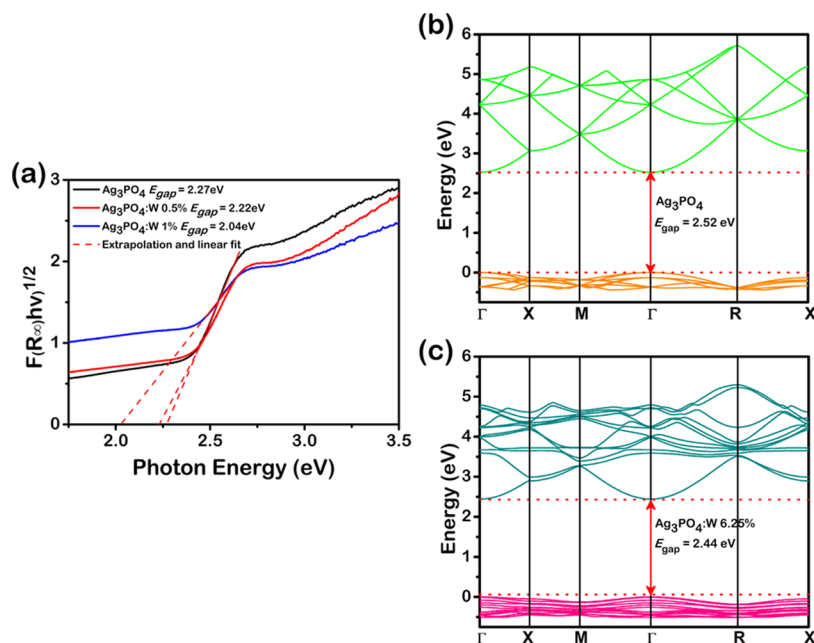
Figure 6. (a) UV−visible absorption spectra and band-gap energies for Ag_3PO_4, Ag_3PO_4:W 0.5%, and Ag_3PO_4:W 1% samples. Calculated band structures of (b) Ag_3PO_4 and (c) Ag_3PO_4:W models.
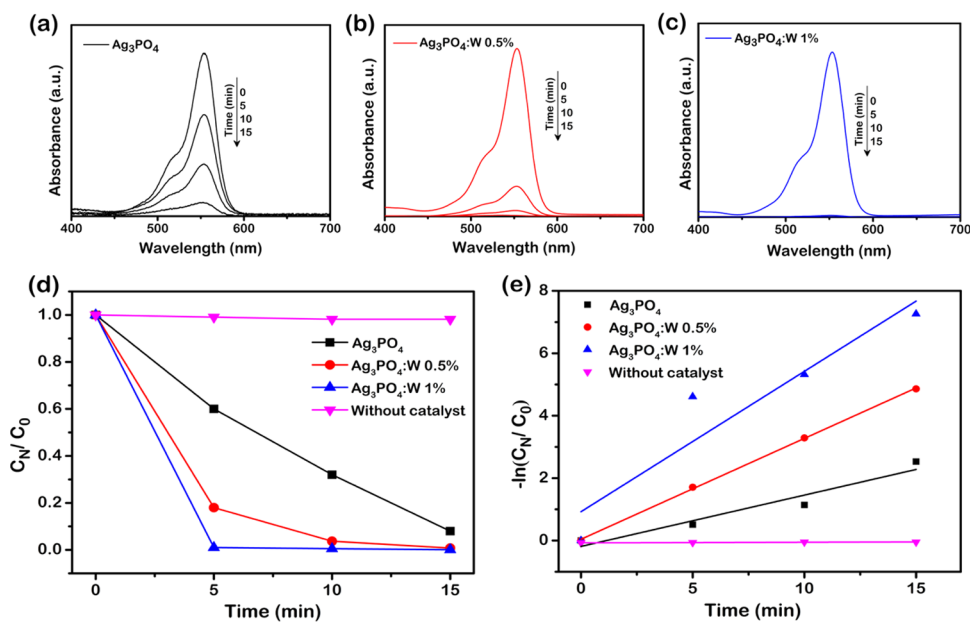

Figure 7. UV−visible absorption spectra of RhB upon photodegradation in the presence of (a) Ag_3PO_4, (b) Ag_3PO_4:W 0.5%, and (c) Ag_3PO_4:W 1%. (d) Photocatalytic degradation of RhB (1.0×10^{-1} mol L^{-1}) in the absence and in the presence of Ag_3PO_4 and Ag_3PO_4 doped with different amounts of W and (e) Langmuir−Hinshelwood plot for the determination of the rate constant.

samples. Considering that Ag_3PO_4 has an indirect band gap,[51] the Kubelka−Munk[52] equation and Tauc method[53] were used to calculate the experimental band-gap energy (E_{gap}) values. The pure Ag_3PO_4 sample presented a E_{gap} value of 2.27 eV, which is consistent with that reported in the literature.[21] It can be noted that with the increase of the doping concentration, there was consequently a decrease in the E_{gap} value from 2.22 eV for the Ag_3PO_4:W 0.5% sample to 2.04 eV for the Ag_3PO_4:W 1% sample. This behavior can be associated with an enhanced structural disorder induced by the W cation in the Ag_3PO_4 lattice, which allows the appearance of new intermediate levels in the forbidden zone between the VB

and CB. This result is consistent with that observed for the Ag_3PO_4:Mo structure,[33] where the doping by Mo also played key roles in the Ag_3PO_4 electronic structure.

From the calculations, we constructed the band structure for the pure Ag_3PO_4 and Ag_3PO_4:W to analyze the electronic properties of the models. Figure 6b,c reveals that both models caused a direct transition between the Γ-points, with E_{gap} values of 2.52 and 2.44 eV, respectively. Therefore, the disorder created by the W doping on the Ag_3PO_4 structure provokes a small decrease of the band gap, which is in agreement with our experimental data. To verify how the atomic orbitals are involved and affected by the W doping in
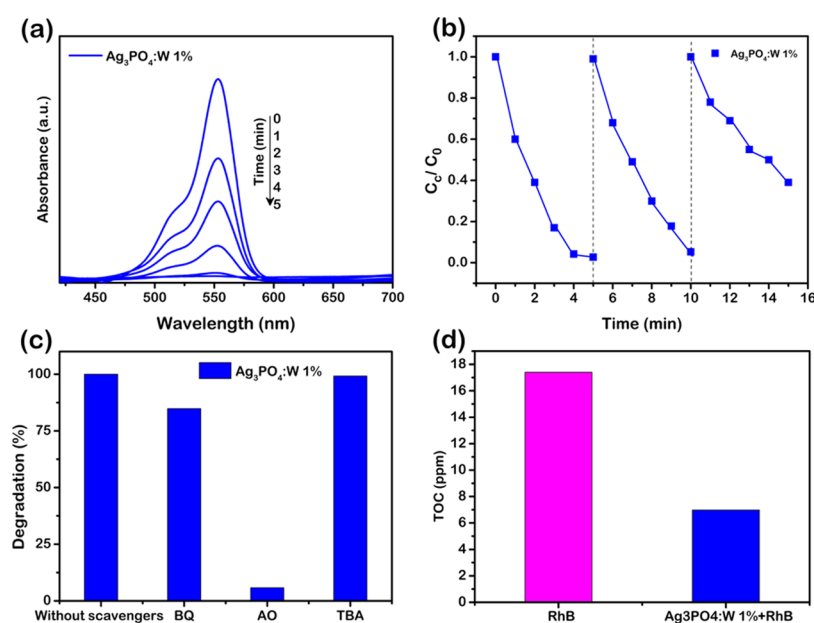
Figure 8. (a) UV−visible absorption spectra of RhB photodegradation in the presence of Ag_3PO_4:W 1% collected in time less than 5 min and (b) run cycles of RhB degradation using Ag_3PO_4:W 1% under visible-light irradiation. (c) Influence of the scavengers on the degradation of RhB in the presence of Ag_3PO_4:W 1% under visible-light irradiation and (d) analysis of total organic carbon (TOC) for degradation of RhB in the presence of Ag_3PO_4:W 1% under 30 min of visible-light irradiation.

the electronic transitions, the density of states (DOS) was analyzed (Figure S7). The VB of pure Ag_3PO_4 is mainly constituted by Ag and O atoms with a small contribution of P atoms with an effective hybridization of the Ag 4d and O 2p orbitals on the top of the VB formed mainly by the ligand orbital. By W doping on the Ag_3PO_4 sample, the top of the VB loses part of the ligand orbital, consequently increasing the antiligand orbital region. This is generally associated with a loss of symmetry in the $[AgO_4]$ clusters. The CB of both models is mostly derived from Ag atoms with a small contribution of P and O atoms as well as W atoms in the Ag_3PO_4:W model. The knowledge of the density of states allows us to explain how the atomic orbitals are involved in the properties of the materials.

Photocatalytic Activity of Ag_3PO_4:W Microcrystals against RhB Dye. Photocatalytic tests were performed for the pure Ag_3PO_4 sample and Ag_3PO_4:W 0.5 and 1% samples by the degradation of RhB under visible-light irradiation. Figure 7a−c shows the UV−visible absorption spectra obtained by collecting aliquots at given times (0, 5, 10, and 15 min) and subsequently measuring their absorbance at 554 nm. Figure 7d shows the variation of RhB concentration (C_N/C_0) as a function of irradiation time, where C_0 and C_N are the equilibrium adsorption concentrations at t_0 and at the irradiation time t, respectively. From the control experiment (without the addition of a photocatalyst), the photolysis of RhB upon visible-light irradiation was almost negligible. The doped samples presented higher photocatalytic activity than the pure material, especially the Ag_3PO_4:W 1% sample, allowing a complete degradation of the dye in less than 5 min of irradiation. The kinetics of the photocatalytic degradation can be described using the pseudo-first-order reaction, and the rate constants (k') for the degradation of RhB with and without the presence of photocatalysts were calculated by the Langmuir−Hinshelwood plot (Figure 7e). As mentioned above, the Ag_3PO_4:W 1% sample revealed a better photocatalytic activity, with a k' of 4.49×10^{-1} min^{-1}, approximately 3 times higher than that of the pure Ag_3PO_4

sample ($k' = 1.64 \times 10^{-1}$ min^{-1}) and even higher than that of the Ag_3PO_4:W 0.5% sample ($k' = 3.23 \times 10^{-1}$ min^{-1}).

To follow more precisely the degradation rate, another experiment was performed with intervals of 1 min for the Ag_3PO_4:W 1% sample, as shown in Figure 8a, revealing a complete degradation in approximately 4 min of irradiation under visible light. This result confirms that the material proposed has promising photocatalytic properties comparable to other efficient Ag_3PO_4 doped photocatalysts. To study the photocatalytic stability of the doped material with W, cycling tests were performed for the same sample (Figure 8b). It can be seen that the doped sample maintains its stability until the second cycle, but its catalytic activity decreases in the third cycle. It is well reported that Ag_3PO_4 undergoes a photo-corrosion process, where the photoexcited electrons cause the reduction of Ag^+ to Ag^0 during the photocatalysis. Ag^0 is formed mainly on the active surfaces of the material, hampering the absorption of light and, thus, decreasing the photocatalytic activity.[54,55] In the Ag_3PO_4:W 1% sample, this mechanism is facilitated since the presence of W dopant causes structural disturbances, generates defects on the particle surface, and consequently changes the surface energy of the microcrystals. These features can reduce the stability of Ag^+ to photocorrosion, as also observed by doping the Ag_3PO_4 structure with Mo.[33] However, even with a loss in photo-catalytic activity, the photocatalyst degrades 60% of the dye within 5 min in the third cycle of reuse.

In general, a complete semiconductor photocatalytic cycle involves light harvesting, photogeneration of charge carriers, charge separation and transfer, and surface redox reactions to allow the formation of reactive oxygen species (ROS) that play crucial roles in photocatalysis.[56,57] Therefore, to understand the photodegradation mechanism of the doped Ag_3PO_4 samples and the higher photocatalytic performance of Ag_3PO_4:W 1%, photocatalytic experiments with radical scavengers were conducted using this sample as a photo-catalyst. As shown in Figure 8c, the addition of AO caused the
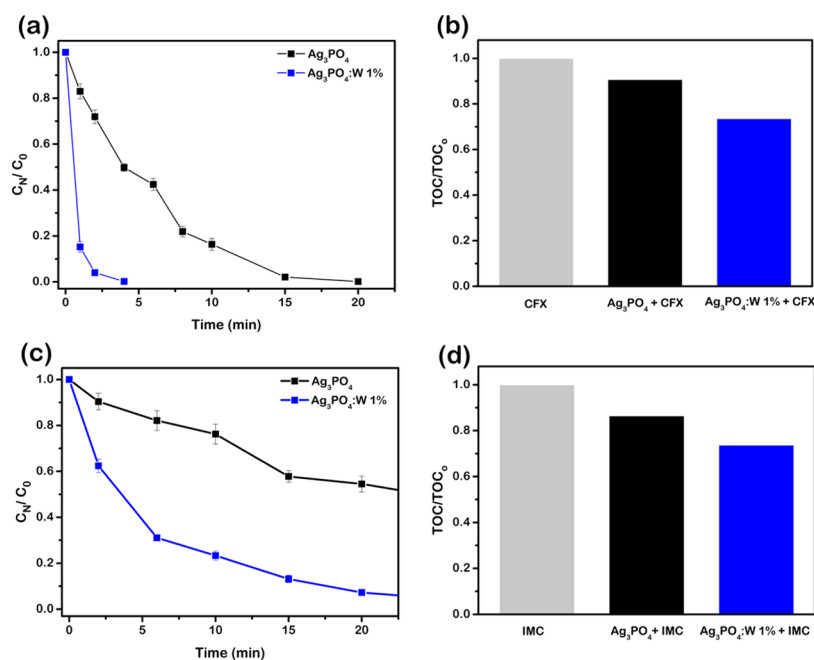
Figure 9. (a) Photocatalytic degradation of CFX in the presence of Ag_3PO_4 and Ag_3PO_4:W 1% in a linear plot and (b) analysis of total organic carbon for degradation of CFX in the presence of Ag_3PO_4 and Ag_3PO_4:W 1% under 30 min of visible-light irradiation. (c) Photocatalytic degradation of IMC in the presence of Ag_3PO_4 and Ag_3PO_4:W 1% in a linear plot and (d) analysis of total organic carbon for degradation of IMC in the presence of Ag_3PO_4 and Ag_3PO_4:W 1% under 30 min of visible-light irradiation.

degradation to decrease from almost 100% to less than 20%, relative to the same visible-light irradiation time, showing that $h^\bullet$ is the major active species in the photodegradation mechanism. The addition of BQ presented a slight influence on the photodegradation efficiency, and the addition of *tert*-butyl alcohol (TBA) did not exhibit significant influence. These results indicate that O_2' and OH* species had, respectively, minor and negligible participation in the observed mechanism. At this point, it is important to remark that the use of electron spin resonance would further confirm the nature of the radicals involved in the degradation process.

To further evaluate the photocatalytic activity of Ag_3PO_4 and Ag_3PO_4:W 1%, the decrease in the total organic carbon (TOC) concentration during the photodegradation processes was also investigated. Because the TOC analyzer has low sensibility, the concentration of contaminant was doubled in these tests (20 mg L^{-1}). Thus, the mass of the catalyst was increased accordingly to 100 mg, and the irradiation time was extended to 30 min. The remaining TOC fraction of the RhB solution can be seen in Figure 8d. As expected for the Ag_3PO_4:W 1% photocatalyst, the TOC removal was much higher than when the pure material was used. In this case, the TOC decreased by 60% after 30 min, indicating that Ag_3PO_4:W 1% could mineralize RhB and its degradation byproducts under visible-light irradiation even in a short time. For the Ag_3PO_4 sample, the degradation percentage was approximately 32%. A similar degradation extent for RhB (~52%) was reported using Ag_3PO_4:Mo 0.5% after 30 min of treatment.[33]

W-doped samples are composed of distorted clusters, which present significant changes in bond lengths and angles with respect to their equilibrium positions (Figure 2b). This symmetry breaking process leads to an electronic reorganization and the spontaneous formation of donor and acceptor levels within the band gap, causing the gradual decrease in the

E_{gap} observed for the W-doped Ag_3PO_4 samples (Figure 6a−c). Hence, the higher amount of dopant in the Ag_3PO_4:W 1% sample results in a greater density of defect-related energy states, which can increase the visible-light absorption, more efficiently serve as charge carrier traps to delay $e'−h^\bullet$ recombination, and consequently improve the photocatalytic property of the material. In addition, the smaller particle sizes of the Ag_3PO_4:W 1% sample (Table 2) also prevent charge carrier recombination, since there is a decrease in the distance for their migration from the core to the surface of the microcrystals. The higher surface area in comparison to the other samples could also develop an additional role for the best RhB degradation observed by increasing the dye adsorption capability of the photocatalyst.

Photocatalytic Activity of Ag_3PO_4:W against CFX and IMC. Once the photocatalytic activity of materials doped with W, especially the sample Ag_3PO_4:W 1%, showed promising results, even better than those seen in Mo-doped Ag_3PO_4,[33] it was also investigated whether this property extends to another class of organic contaminants. For this, additional experiments were carried out for the highest active photocatalyst (Ag_3PO_4:W 1%) to test the photodegradation of CFX and IMC insecticide solutions. As can be seen in Figure 9a, a behavior similar to that of RhB was found in the photodegradation of CFX, using the pure and doped material. The total removal of CFX was achieved after 20 min using Ag_3PO_4 against 4 min using the W-doped material. The conversion to CO_2 is also superior for Ag_3PO_4:W 1% (28%) than for pure Ag_3PO_4 (10%), as shown by the mineralization analysis in Figure 9b. On the other hand, the lower efficiency of Ag_3PO_4:W 1% compared to its yield in RhB mineralization (60%) indicates that, for CFX, the degradation of byproducts is more recalcitrant than that of the original molecule. A similar result about the tardive mineralization process of antibiotics was published by Chen et al.,[58] in which the photocatalytic

mineralization of ciprofloxacin (1 mg L^{-1}) using Gab/Ag_3PO_4/hematite under solar light was ~30% in 30 min.

Figure 9c shows the evolution of the IMC concentration as a function of time of irradiation for the photocatalysts used. In this case, a moderate removal of IMC (~55%) was achieved after 30 min using the pure Ag_3PO_4 sample, suggesting that the IMC molecule is recalcitrant toward oxidation provoked by the use of this material. Clearly, a significant improvement in the IMC degradation was obtained using Ag_3PO_4:W 1%, where almost 100% removal of insecticide was achieved after 30 min. However, the degradation of IMC did not result in significant levels of mineralization in the time interval probed but only in accumulation of byproducts in the reaction medium, as shown in Figure 9d. For the pure and 1% doped materials, the degradation was ~14 and ~26%, respectively.

These results evidenced that some of the degradation byproducts are more stable toward the photocatalytic process, as also observed elsewhere.[59,60] Specifically, Katsumata et al. found a high level of conversion to CO_2 (83%) in the photocatalytic treatment of bisphenol A (10 mg L^{-1}) using Ag_3PO_4 under visible light after 180 min.[61] This indicates that for the Ag_3PO_4:W 1% sample, the mineralization level obtained for CFX and IMC could be improved by increasing the irradiation time. Hence, it clearly appears that the Ag_3PO_4:W 1% sample has superior photocatalytic properties compared to the pure material and thus could be an interesting option to degrade a wide range of pollutants.

Antibacterial Activity. Antimicrobial resistance is one of the most difficult issues humanity deals with, and the World Health Organization (WHO) has been emphasizing the urgency of new options of treatments with low resistance development.[62] In this sense, there is a need to develop novel antibacterial agents to combat bacteria, such as *Staphylococcus aureus*, which has the ability to develop resistance to all classes of clinically available antibiotics and is often detected in both hospital and municipal wastewaters.[63] Although some previous studies successfully demonstrated the antibacterial capacity of compounds such as Ag_3PO_4,[13,15,16] this is the first time that the Ag_3PO_4:W activity is reported against methicillin-resistant *S. aureus* (MRSA). Antibacterial tests were performed using pure Ag_3PO_4 and W-doped Ag_3PO_4 samples, and the results are displayed in Figure 10. All probed materials showed antimicrobial activity against MRSA, and the minimal inhibitory and minimal bactericidal concentration (MIC/MBC) values for the Ag_3PO_4, Ag_3PO_4:W 0.5%, and Ag_3PO_4:W 1% samples were 125, 31.25, and 7.81 $\mu g\ mL^{-1}$,

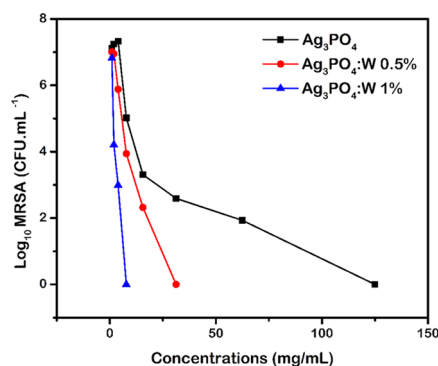**Figure 10.** Bacterial growth values (Log_{10}) as a function of the concentrations (mg mL^{-1}) of Ag_3PO_4 and Ag_3PO_4:W.

respectively. It can be observed that the antibacterial capacity of the material increases as the W concentration increases.

The substitution of P^{5+} by W^{6+} yields a decrease in particle size and a consequent increase in surface area (Table 2), which could be the main cause for the excellent bactericidal activity of the Ag_3PO_4:W 1% sample. It is known that smaller materials have high antimicrobial capacities in comparison with larger materials,[64] and the increase in the surface area of the particles holds the advantage of efficiently binding to microorganisms for enhanced antimicrobial action.[65] Wu et al.[13] observed the correlation among particle size, specific surface area, and antibacterial activity in Ag_3PO_4 micro- and nanoparticles. In this case, as the particle size decreased, the specific surface area increased, consequently enhancing the antibacterial activity against *Escherichia coli* and *Bacillus subtilis*.

The results obtained through the Rietveld refinement complemented by the theoretical results show that the tetrahedral $[WO_4]$ cluster presented a distorted nature and exhibited longer bond length than the $[PO_4]$ cluster of the pure Ag_3PO_4. The increase of this structural local disorder profoundly alters the properties of the material, leading to an enhanced $e'-h^\bullet$ separation, which is directly proportional to the ROS production.[66] These species, in turn, are responsible for injuries to the plasmatic membrane of microorganisms and changes in the cytoplasmic region, rendering them inhomogeneous in comparison with healthy microorganisms. ROS is also associated with disintegration of DNA, RNA, and microbial proteins, causing severe cellular injuries, making them unviable.[67] Thus, as Ag_3PO_4:W 1% has a greater density of defects, the $e'-h^\bullet$ separation is facilitated, and it becomes the best and most effective antimicrobial agent.

Based on the photocatalytic and bactericidal results, it can be assumed that the proposed W-doped Ag_3PO_4 microcrystals have the potential to be industrially used as a catalyst for wastewater decontamination from organic pollutants, employing sunlight irradiation for these processes, as well as to act as a bactericidal agent for the inactivation of resistant bacteria in wastewater or in product packaging. Both properties were proven to be superior to those of the pure material. However, although higher RhB degradation is detected in the third cycle of reusing the Ag_3PO_4:W 1% sample in comparison with pure Ag_3PO_4, the recycling efficiency improvement of the W-containing microcrystals is still an issue that needs to be addressed to achieve a better stability for this photocatalyst.

■ CONCLUSIONS

In summary, new single-phased photocatalysts based on Ag_3PO_4 doped with W were easily obtained by the chemical precipitation method without any evidence of W dopant segregation up to 1% of doping. The experimental results and first-principles calculations revealed that the structural disorder and morphological changes caused by W incorporation in the Ag_3PO_4 crystalline lattice are closely related to the final properties of the materials, and the Ag_3PO_4:W 1% sample stood out with respect to its photocatalytic and bactericidal activities. In this sense, the Ag_3PO_4:W 1% sample exhibited a remarkable enhancement of photodegradation of RhB with a total discoloration of the dye in only 4 min (90% in 15 min for pure Ag_3PO_4) and a TOC decrease of 60% in 30 min (32% in 30 min for pure Ag_3PO_4). Tests for the photodegradation of antibiotic CFX and insecticide IMC also revealed that Ag_3PO_4:W 1% microcrystals are more interesting to degrade a wide range of pollutants than pure Ag_3PO_4. The bactericidal

activity of the materials was investigated against MRSA. The MIC/MBC value for Ag_3PO_4:W 1% was 7.81 μg mL^{-1}, which is significantly lower in comparison to that of pure Ag_3PO_4 (125 μg mL^{-1}), evidencing the highest potential for the W-doped material to be used as an antimicrobial agent. The present results provide a deep understanding of the photocatalytic and antibacterial activities of Ag_3PO_4:W, standing as a potential material for applications in environmental remediation.

■ EXPERIMENTAL SECTION

Synthesis of Pure Ag_3PO_4 and Ag_3PO_4:W Microcrystals. Pure Ag_3PO_4 and Ag_3PO_4:W samples were synthesized by the CP method in aqueous medium at room temperature. The salts used in the preparation of the materials were $(NH_4)_2HPO_4$ (0.001 M) (98.6%, J.T. Baker), $AgNO_3$ (0.003 M) (99.8%, Vetec), and $Na_2WO_4 \cdot 2H_2O$ (99.5%, Sigma-Aldrich). Two solutions were prepared: the first one was $(NH_4)_2HPO_4$ diluted in 50 mL of deionized water at 30 °C under agitation to dissolve the salt and the second one was composed of $AgNO_3$ diluted in 50 mL of deionized water at 30 °C under stirring. The dopant was added in the first solution after complete dissolution of the $(NH_4)_2HPO_4$ salt. The salt contents used were 0.000, 0.005, 0.01, and 0.02 moles. The syntheses were conducted by first adding the second solution to the first one and then keeping this mixture under stirring for 10 min to obtain yellow precipitates. The obtained materials were centrifuged several times with deionized water to remove soluble species and oven-dried at 60 °C for 24 h. For practical reasons, these samples were named pure Ag_3PO_4 and Ag_3PO_4:W 0.5, 1, and 2%.

Characterization Techniques. The obtained materials were characterized by XRD using a D/Max-2500PC diffractometer (Rigaku, Japan) with Cu $K\alpha_1$ radiation (λ = 1.54056 Å) in the 2θ range of 10−100°, a scanning speed of 1° min^{-1}, and a step size of 0.02°. For the Rietveld refinements, we used the general structural analysis system (GSAS) software package with graphic interface EXPGUI. The theoretical diffraction pattern was obtained from ICSD no. 14000, which is based on the body-centered cubic structure with the $P\bar{4}3n$ space group. For the micro-Raman spectra, an iHR550 spectrometer (Horiba Jobin-Yvon, Japan) was used coupled to a CCD detector and an argon ion laser (Melles Griot) operating at 514.5 nm with a maximum power of 200 mW. The spectra were measured in the range of 50−1100 cm^{-1}. Measurements of X-ray photoelectron spectroscopy (XPS) were performed on a Scienta Omicron ESCA+ spectrometer (Germany) using monochromatic Al $K\alpha$ (1486.7 eV). The maximum deconvolution was performed using a line of 70% Gaussian and 30% Lorentzian with a baseline of the nonlinear (Shirley-type) sigmoid. For calibration of the binding energy of the elements, the peak C 1s at 248.8 eV was used as reference. Transmission electron microscopy (TEM) and high-resolution TEM (HR-TEM) were performed using an FEI Tecnai G2F20 microscope (Netherlands) operating at 200 kV. A high-angle annular dark-field (HAADF) image and elemental mapping by energy-dispersive X-ray spectroscopy (EDS) were recorded in the scanning TEM (STEM) mode. The morphologies of the samples were characterized by field emission gun scanning electron microscopy (FESEM) in an FEI instrument (Inspection Model F50) operating at 10 kV. The BET surface area (S_{BET}) and particle sizes of the samples were studied using N_2 adsorption and desorption isotherms measured at 77 K on

a Micrometrics ASAP 2420 A surface area and porosimetry analyzer. Prior to the N_2 adsorption measurement, the samples were degassed at 200 °C under vacuum for 4 h. The S_{BET} of the samples was calculated using the Brunauer−Emmett−Teller (BET) method in the relative pressure (P/P_0) range of 0.05−0.16. To obtain ultraviolet−visible (UV−visible) absorption spectra, a Varian Cary 5G spectrophotometer was used in diffuse reflection mode.

Computational Methods. First-principles calculations for the Ag_3PO_4 and Ag_3PO_4:W structures were performed using the CRYSTAL14 software package.[68,69] Moreover, density functional theory (DFT) calculations at the B3LYP hybrid functional level were made.[70,71] The thresholds controlling the accuracy of Coulomb's law calculations and the exchange integrals were set to 10^{-8}, 10^{-8}, 10^{-8}, 10^{-8}, and 10^{-14}, and the percentage of Fock/Kohn−Sham matrix mixing was set to 40. The diagonalization of the Fock matrix was performed using an adequate number of k-point grids in the reciprocal space. The basis sets obtained from the CRYSTAL website[72] for the atomic centers of Ag, P, O, and W were described by PS-311d31G, 85-21d1G, 6-31d1, and PS-311(d31)G, respectively, where PS stands for Hay and Wadt's nonrelativistic small-core pseudopotential.[73] The lattice parameters and internal atomic coordinates of the bulk Ag_3PO_4 were fully optimized until all force components were less than 10^{-6} eV $Å^{-2}$. From these optimized parameters, two $2 \times 2 \times 2$ supercell periodic models were built for pure Ag_3PO_4 and Ag_3PO_4:W samples to accurately describe the structural and electronic properties derived from the experimental synthesis. In the supercell model, there were 16 Ag_3PO_4 units (Z = 16). To build the Ag_3PO_4:W model, one P cation was replaced by one W cation. Therefore, it was necessary to create a load balance to ensure the electroneutrality of the system by generating a Ag^+ vacancy near the P atom replaced by the W atom. Our Ag_3PO_4:W model contains 6.25 mol % W in the structure. Unfortunately, to obtain lower percentages of W doping, a larger supercell model would be required, and the computational cost is prohibitive. The same theoretical strategy was used to construct an Ag_3PO_4:Mo model, as recently reported.[33] The band structure and density-of-states (DOS) models were constructed along the appropriate high-symmetry directions of the corresponding irreducible Brillouin zone implemented in the CRYSTAL program.

Photocatalytic Measurements. The photocatalytic activity of both pure and doped samples was tested for degradation of RhB (95%, Aldrich) under visible-light irradiation. For the tests, 50 mg of each photocatalyst, Ag_3PO_4 and Ag_3PO_4:W, was added in a beaker containing a solution of RhB (50 mL, 10 mg L^{-1}). This solution was placed in an ultrasonic bath (Branson, model 1510; frequency 42 kHz) for 30 min and then stirred for another 30 min for a better absorption−adsorption equilibrium process, always keeping the solutions protected from light. After this stage, an aliquot at time 0 was collected, the solution was placed under irradiation of six lamps (Philips TL-D, 15 W), and the system was kept under stirring at a controlled temperature of 20 °C. Subsequent aliquots were collected at determined intervals and centrifuged to remove the photocatalyst powder. Dye degradation was monitored by measuring the peak absorbance of RhB (λ_{max} = 554 nm) using a UV−visible spectrophotometer (V-660, JASCO). A control experiment was carried out under the same conditions but without photocatalysts.

To understand the roles of reactive oxygen species (ROS) in the photocatalytic process, experiments on scavengers were performed by adding 0.1 M *tert*-butyl alcohol (TBA) (Alfa Aesar), 1×10^{-3} M ammonium oxalate (AO) (Alfa Aesar), and 1×10^{-3} M benzoquinone (BQ) (Alfa Aesar) as scavengers of the hydroxyl radical (OH*), hole (h$^{\bullet}$,), and superoxide radical (O$_2'$), respectively.

In addition, we studied the efficiency of this novel material regarding the oxidation of another class of contaminant, i.e., the degradation process of synthetic solutions (10 mg L^{-1}) of CFX (95%, Vita Nova) and IMC (commercial solution, AdamaBrasil), which are types of antibiotic and insecticide, respectively. The CFX and IMC concentrations were monitored by high-performance liquid chromatography (HPLC) using Shimadzu LC-20A equipment and a reversed-phase C18 column (150 mm × 4.6 mm, 5 μm particle size from Phenomenex) as the stationary phase. For CFX determination, a mixture of 10 mmol L^{-1} KH$_2$PO$_4$ (eluent A) buffer solution (pH 3, adjusted with phosphoric acid) and methanol (eluent B) was used as the mobile phase at 1.0 mL min^{-1}, with the following gradient elution protocol: from 10% (V/V) eluent B to 90% in 10 min and then returning to 10% in 3 min. CFX was detected at 262 nm, and the injection volume was 15 μL. A mixture of 0.1% formic acid (eluent A) and methanol (eluent B) at 1.0 mL min^{-1} in gradient mode was used as the mobile phase for the IMC determination: from 20% (V/V) eluent B to 90% in 8 min and then returning to 20% in 3 min. IMC was detected at 270 nm, and the injection volume was 25 μL.

Finally, the mineralization (i.e., conversion to CO$_2$) extent was also measured by analysis of the total organic carbon (TOC) concentration (TOC analyzer, GE Sievers Innovox) using 6 mol L^{-1} H$_3$PO$_4$ (a.r., Mallinckrodt) and 30% (m/m) Na$_2$S$_2$O$_8$ (99%, Sigma-Aldrich) as acidifier and oxidant reagents, respectively.

Antibacterial Measurements. In this study, the antibacterial activity of Ag$_3$PO$_4$ and Ag$_3$PO$_4$:W was investigated against MRSA from the American Type Culture Collection (ATCC 33591). Antibacterial activity probes were performed according to the protocol previously described.[74] Briefly, MRSA cells were cultured from the frozen stock onto Mueller—Hinton agar plates and incubated at 37 °C for 24 h. Colonies of fresh cells were transferred to tryptic soy broth (TSB) and incubated until reaching the mid-log stage of microbial growth. The minimal inhibitory and minimal bactericidal concentration (MIC/MBC) susceptibility tests were performed using the broth microdilution method of the Clinical and Laboratory Standards Institute, documents M27-A3 (2008),[75] with some modifications. Microbial growth control consisted of bacterial suspension in culture medium without particles, while negative controls consisted of uninoculated culture medium.[76] To ensure data reproducibility, the experiments were performed in triplicate, on three different occasions.

ASSOCIATED CONTENT

Ⓢ Supporting Information

The Supporting Information is available free of charge at https://pubs.acs.org/doi/10.1021/acsomega.0c03019.

> Rietveld refinement plots; crystal data from Rietveld refinements; high-resolution XPS spectra of Ag 3d, O 1s, and P 2p; particle size distributions; adsorption— desorption isotherms; and density-of-state models (PDF)

AUTHOR INFORMATION

Corresponding Authors

Aline B. Trench — *CDMF—Department of Chemistry, Federal University of São Carlos, 13565-905 São Carlos, SP, Brazil;* Email: aline_trench@hotmail.com

Thales R. Machado — *CDMF—Department of Chemistry, Federal University of São Carlos, 13565-905 São Carlos, SP, Brazil;* orcid.org/0000-0002-3246-6329; Email: tmachado.quimica@gmail.com

Elson Longo — *CDMF—Department of Chemistry, Federal University of São Carlos, 13565-905 São Carlos, SP, Brazil;* orcid.org/0000-0001-8062-7791; Email: elson.liec@gmail.com

Authors

Amanda F. Gouveia — *Institute of Chemistry, State University of Campinas, 13083-970 Campinas, SP, Brazil;* orcid.org/0000-0003-3441-3674

Camila C. Foggi — *CDMF—Department of Chemistry, Federal University of São Carlos, 13565-905 São Carlos, SP, Brazil;* orcid.org/0000-0002-1210-1234

Vinícius Teodoro — *CDMF—Department of Chemistry, Federal University of São Carlos, 13565-905 São Carlos, SP, Brazil*

Isaac Sánchez-Montes — *Department of Chemistry, Federal University of São Carlos, 13565-905 São Carlos, SP, Brazil*

Mayara M. Teixeira — *CDMF—Department of Chemistry, Federal University of São Carlos, 13565-905 São Carlos, SP, Brazil;* orcid.org/0000-0001-9038-0024

Letícia G. da Trindade — *Department of Chemistry, São Paulo State University, 17033-360 Bauru, SP, Brazil*

Natalia Jacomaci — *Chemistry Institute, São Paulo State University, 14800-060 Araraquara, SP, Brazil*

Andre Perrin — *University of Rennes 1, F-35042 Rennes-Cedex, France*

Christiane Perrin — *University of Rennes 1, F-35042 Rennes-Cedex, France*

Jose M. Aquino — *Department of Chemistry, Federal University of São Carlos, 13565-905 São Carlos, SP, Brazil*

Juan Andrés — *Department of Analytical and Physical Chemistry, University Jaume I, 12071 Castellón, Spain;* orcid.org/0000-0003-0232-3957

Complete contact information is available at:
https://pubs.acs.org/10.1021/acsomega.0c03019

Author Contributions

The manuscript was written through contributions of all authors. All authors have given approval to the final version of the manuscript.

Notes

The authors declare no competing financial interest.

ACKNOWLEDGMENTS

■ REFERENCES

(1) Zhang, S.; Li, B.; Wang, X.; Zhao, G.; Hu, B.; Lu, Z.; Wen, T.; Chen, J.; Wang, X. Recent Developments of Two-dimensional Graphene-based Composites in Visible-light Photocatalysis for Eliminating Persistent Organic Pollutants from Wastewater. *Chem. Eng. J.* **2020**, *390*, No. 124642.

(2) Chen, Z.; Zhang, S.; Liu, Y.; Alharbi, N. S.; Rabah, S. O.; Wang, S.; Wang, X. Synthesis and Fabrication of g-C_3N_4-based Materials and Their Application in Elimination of Pollutants. *Sci. Total Environ.* **2020**, *731*, No. 139054.

(3) Fujishima, A.; Honda, K. Electrochemical Photolysis of Water at a Semiconductor Electrode. *Nat. Mater.* **1972**, *238*, 37−38.

(4) Chen, X.; Zhang, Z.; Chi, L.; Nair, A. K.; Shangguan, W.; Jiang, Z. Recent Advances in Visible-light-driven Photoelectrochemical Water Splitting: Catalyst Nanostructures and Reaction Systems. *Nano-Micro Lett.* **2016**, *8*, 1−12.

(5) Li, X.; Li, J.; Bai, J.; Dong, Y.; Li, L.; Zhou, B. The Inhibition Effect of Tert-butyl Alcohol on the TiO_2 Nano Assays Photo-electrocatalytic Degradation of Different Organics and Its Mechanism. *Nano-Micro Lett.* **2016**, *8*, 221−231.

(6) Li, X.; Jiang, Y.; Cheng, W.; Li, Y.; Xu, X.; Lin, K. Mesoporous TiO_2/Carbon Beads: One-pot Preparation and their Application in Visible-light-induced Photodegradation. *Nano-Micro Lett.* **2015**, *7*, 243−254.

(7) Kim, H. G.; Hwang, D. W.; Lee, J. S. An Undoped, Single-phase Oxide Photocatalyst Working under Visible Light. *J. Am. Chem. Soc.* **2004**, *126*, 8912−8913.

(8) Martin, D. J.; Liu, G.; Moniz, S. J.; Bi, Y.; Beale, A. M.; Ye, J.; Tang, J. Efficient Visible Driven Photocatalyst, Silver Phosphate: Performance, Understanding and Perspective. *Chem. Soc. Rev.* **2015**, *44*, 7808−7828.

(9) Dong, L.; Wang, P.; Wang, S.; Lei, P.; Wang, Y. A Simple Way for Ag_3PO_4 Tetrahedron and Tetrapod Microcrystals with High Visible-light-responsive Activity. *Mater. Lett.* **2014**, *134*, 158−161.

(10) Liang, Q.; Ma, W.; Shi, Y.; Li, Z.; Yang, X. Hierarchical Ag_3PO_4 Porous Microcubes with Enhanced Photocatalytic Properties Synthesized with the Assistance of Trisodium Citrate. *CrystEngComm* **2012**, *14*, 2966−2973.

(11) Yi, Z.; Ye, J.; Kikugawa, N.; Kako, T.; Ouyang, S.; Stuart-Williams, H.; Yang, H.; Cao, J.; Luo, W.; Li, Z.; Liu, Y.; Withers, R. L. An Orthophosphate Semiconductor with Photooxidation Properties under Visible-light Irradiation. *Nat. Mater.* **2010**, *9*, 559−564.

(12) Hsieh, M. S.; Su, H. J.; Hsieh, P. L.; Chiang, Y. W.; Huang, M. H. Synthesis of Ag_3PO_4 Crystals with Tunable Shapes for Facet-dependent Optical Property, Photocatalytic Activity, and Electrical Conductivity Examinations. *ACS Appl. Mater. Interfaces* **2017**, *9*, 39086−39093.

(13) Wu, A.; Tian, C.; Chang, W.; Hong, Y.; Zhang, Q.; Qu, Y.; Fu, H. Morphology-controlled Synthesis of Ag_3PO_4 Nano/microcrystals and their Antibacterial Properties. *Mater. Res. Bull.* **2013**, *48*, 3043−3048.

(14) Liu, J.-K.; Luo, C.-X.; Wang, J.-D.; Yang, X.-H.; Zhong, X.-H. Controlled Synthesis of Silver Phosphate Crystals with High Photocatalytic Activity and Bacteriostatic Activity. *CrystEngComm* **2012**, *14*, 8714.

(15) Deng, C.-H.; Gong, J.-L.; Ma, L.-L.; Zeng, G.-M.; Song, B.; Zhang, P.; Huan, S.-Y. Synthesis, Characterization and Antibacterial Performance of Visible Light-responsive Ag_3PO_4 Particles Deposited on Graphene Nanosheets. *Process Saf. Environ. Prot.* **2017**, *106*, 246−255.

(16) Seo, Y.; Yeo, B.-E.; Cho, Y.-S.; Park, H.; Kwon, C.; Huh, Y.-D. Photo-enhanced Antibacterial Activity of Ag_3PO_4. *Mater. Lett.* **2017**, *197*, 146−149.

(17) Zhang, Y.; Zhang, X.; Hu, R.; Yang, Y.; Li, P.; Wu, Q. Bifunctional Nano-Ag_3PO_4 with Capabilities of Enhancing Ceftazidime for Sterilization and Removing Residues. *RSC Adv.* **2019**, *9*, 17913−17920.

(18) Shao, J.; Ma, J.; Lin, L.; Wang, B.; Jansen, J. A.; Walboomers, X. F.; Zuo, Y.; Yang, F. Three-dimensional Printing of Drug-loaded Scaffolds for Antibacterial and Analgesic Applications. *Tissue Eng., Part C* **2019**, *25*, 222−231.

(19) Weng, B.; Qi, M.-Y.; Han, C.; Tang, Z.-R.; Xu, Y.-J. Photocorrosion Inhibition of Semiconductor-based Photocatalysts: Basic Principle, Current Development, and Future Perspective. *ACS Catal.* **2019**, *9*, 4642−4687.

(20) Zwara, J.; Grabowska, E.; Klimczuk, T.; Lisowski, W.; Zaleska-Medynska, A. Shape-dependent Enhanced Photocatalytic Effect under Visible Light of Ag_3PO_4 Particles. *J. Photochem. Photobiol., A* **2018**, *367*, 240−252.

(21) Chen, X.; Dai, Y.; Wang, X. Methods and Mechanism for Improvement of Photocatalytic Activity and Stability of Ag_3PO_4: A Review. *J. Alloys Compd.* **2015**, *649*, 910−932.

(22) Li, X.; Xu, P.; Chen, M.; Zeng, G.; Wang, D.; Chen, F.; Tang, W.; Chen, C.; Zhang, C.; Tan, X. Application of Silver Phosphate-based Photocatalysts: Barriers and Solutions. *Chem. Eng. J.* **2019**, *366*, 339−357.

(23) Zhang, S.; Zhang, S.; Song, L. Super-high Activity of Bi^{3+} Doped Ag3PO4 and Enhanced Photocatalytic Mechanism. *Appl. Catal., B* **2014**, *152−153*, 129−139.

(24) Afif, M.; Sáulaeman, U.; Riapanitra, A.; Andreas, R.; Yin, S. Use of Mn Doping to Suppress Defect Sites in Ag_3PO_4: Applications in Photocatalysis. *Appl. Surf. Sci.* **2019**, *466*, 352−357.

(25) Yu, H.; Kang, H.; Jiao, Z.; Lü, G.; Bi, Y. Tunable Photocatalytic Selectivity and Stability of Ba-doped Ag_3PO_4 Hollow Nanosheets. *Chin. J. Catal.* **2015**, *36*, 1587−1595.

(26) Song, L.; Chen, Z.; Li, T.; Zhang, S. A Novel Ni^{2+}-doped Ag_3PO_4 Photocatalyst with High Photocatalytic Activity and Enhancement Mechanism. *Mater. Chem. Phys.* **2017**, *186*, 271−279.

(27) Cao, W.; Gui, Z.; Chen, L.; Zhu, X.; Qi, Z. Facile Synthesis of Sulfate-doped Ag_3PO_4 with Enhanced Visible Light Photocatalystic Activity. *Appl. Catal., B* **2017**, *200*, 681−689.

(28) Luo, J.; Luo, Y.; Li, Q.; Yao, J.; Duan, G.; Liu, X. Synthesis of Doughnut-like Carbonate-doped Ag_3PO_4 with Enhanced Visible Light Photocatalytic Activity. *Colloids Surf., A* **2017**, *535*, 89−95.

(29) Liu, X.; Ma, R.; Zhuang, L.; Hu, B.; Chen, J.; Liu, X.; Wang, X. Recent Developments of Doped g-C_3N_4 Photocatalysts for the Degradation of Organic Pollutants. *Crit. Rev. Environ. Sci. Technol.* **2020**, 1−40.

(30) Botelho, G.; Andres, J.; Gracia, L.; Matos, L. S.; Longo, E. Photoluminescence and Photocatalytic Properties of Ag_3PO_4 Microcrystals: An Experimental and Theoretical Investigation. *ChemPlusChem* **2016**, *81*, 202−212.

(31) Botelho, G.; Sczancoski, J. C.; Andres, J.; Gracia, L.; Longo, E. Experimental and Theoretical Study on the Structure, Optical Properties, and Growth of Metallic Silver Nanostructures in Ag_3PO_4. *J. Phys. Chem. C* **2015**, *119*, 6293−6306.

(32) Cruz-Filho, J. F.; Costa, T. M. S.; Lima, M. S.; Silva, L. J.; Santos, R. S.; Cavalcante, L. S.; Longo, E.; Luz, G. E. Effect of Different Synthesis Methods on the Morphology, Optical Behavior, and Superior Photocatalytic Performances of Ag_3PO_4 Sub-micro-crystals using White-light-emitting Diodes. *J. Photochem. Photobiol., A* **2019**, *377*, 14−25.

(33) Trench, A. B.; Machado, T. R.; Gouveia, A. F.; Assis, M.; da Trindade, L. G.; Santos, C.; Perrin, A.; Perrin, C.; Oliva, M.; Andrés,

J.; Longo, E. Connecting Structural, Optical, and Electronic Properties and Photocatalytic Activity of Ag_3PO_4:Mo Complemented by DFT Calculations. *Appl. Catal., B* **2018**, *238*, 198−211.

(34) Hussien, M. S. A.; Yahia, I. S. Visible Photocatalytic Performance of Nanostructured Molybdenum-doped Ag_3PO_4: Doping Approach. *J. Photochem. Photobiol., A* **2018**, *356*, 587−594.

(35) Li, H.; Zhang, Y.; Zhang, Q.; Wang, Y.; Fan, Y.; Gao, X.; Niu, J. Boosting Visible-light Photocatalytic Degradation of Indomethacin by an Efficient and Photostable Ag_3PO_4/NG/WO_3 Composites. *Appl. Surf. Sci.* **2019**, *490*, 481−491.

(36) Lu, J.; Wang, Y.; Liu, F.; Zhang, L.; Chai, S. Fabrication of a Direct Z-scheme Type WO_3/Ag_3PO_4 Composite Photocatalyst with Enhanced Visible-light Photocatalytic Performances. *Appl. Surf. Sci.* **2017**, *393*, 180−190.

(37) Shi, H.; Yang, S.; Han, C.; Niu, Z.; Li, H.; Huang, X.; Ma, J. Fabrication of Ag/Ag_3PO_4/WO_3 Ternary Nanoparticles as Superior Photocatalyst for Phenol Degradation under Visible light Irradiation. *Solid State Sci.* **2019**, *96*, No. 105967.

(38) Helmholz, L. The Crystal Structure of Silver Phosphate. *J. Chem. Phys.* **1936**, *4*, 316−322.

(39) Masse, R.; Tordjman, I.; Durif, A. Refinement of Crystal-structure of Silver Monophosphate, Ag_3PO_4-Existence of High-temperature Form. *Z. Kristallogr.* **1976**, *144*, 76−81.

(40) Ng, H. N.; Calvo, C.; Faggiani, R. A New Investigation of the Structure of Silver Orthophosphate. *Acta Crystallogr. B* **1978**, *34*, 898−899.

(41) Deschizeaux-Chéruy, M. N.; Aubert, J. J.; Joubert, J. C.; Capponi, J. J.; Vincent, H. Relation entre Structure et Conductivite Ionique Basse Temperature de Ag_3PO_4. *Solid State Ionics* **1982**, *7*, 171−176.

(42) Katsumata, H.; Sakai, T.; Suzuki, T.; Kaneco, S. Highly Efficient Photocatalytic Activity of g-C_3N_4/Ag_3PO_4 Hybrid Photocatalysts through Z-scheme Photocatalytic Mechanism under Visible Light. *Ind. Eng. Chem. Res.* **2014**, *53*, 8018−8025.

(43) Herschbach, D. R.; Laurie, V. W. Anharmonic Potential Constants and their Dependence upon Bond Length. *J. Chem. Phys.* **1961**, *35*, 458−464.

(44) Zavitsas, A. A. Factors Affecting the Relation between Stretching Frequencies and Bond Lengths. Diatomic and polyatomic species without adjustable fitting parameters. *Spectrochim. Acta, Part A* **2015**, *151*, 553−565.

(45) Holland, P. L. Metal-dioxygen and Metal-dinitrogen Complexes: Where are the Electrons? *Dalton Trans.* **2010**, *39*, 5415−5425.

(46) Bertus, L. M.; Faure, C.; Danine, A.; Labrugere, C.; Campet, G.; Rougier, A.; Duta, A. Synthesis and Characterization of WO_3 thin Films by Surfactant Assisted Spray Pyrolysis for Electrochromic Applications. *Mater. Chem. Phys.* **2013**, *140*, 49−59.

(47) Liu, Y.; Fang, L.; Lu, H.; Li, Y.; Hu, C.; Yu, H. One-pot Pyridine-assisted Synthesis of Visible-light-driven Photocatalyst Ag/Ag_3PO_4. *Appl. Catal., B* **2012**, *115−116*, 245−252.

(48) Zhang, H.; Wang, G.; Chen, D.; Lv, X.; Li, J. Tuning Photoelectrochemical Performances of Ag-TiO_2 Nanocomposites via Reduction/Oxidation of Ag. *Chem. Mater.* **2008**, *20*, 6543−6549.

(49) Cheng, Z.; Bing, F.; Liu, Q.; Zhang, Z.; Fang, X. Novel Z-scheme Visible-light-driven Ag_3PO_4/Ag/SiC Photocatalysts with Enhanced Photocatalytic Activity. *J. Mater. Chem. A* **2014**, *3*, 1−3.

(50) Xu, Y.-S.; Zhang, W.-D. Morphology-controlled Synthesis of Ag_3PO_4 Microcrystals for High Performance Photocatalysis. *CrystEngComm* **2013**, *15*, 5407.

(51) Ma, X.; Lu, B.; Li, D.; Shi, R.; Pan, C.; Zhu, Y. Origin of Photocatalytic Activation of Silver Orthophosphate from First-principles. *J. Phys. Chem. C* **2011**, *115*, 4680−4687.

(52) Kubelka, P.; Munk, F. Ein Beitrag zur Optik der Farbanstriche. *Z. Tech. Phys.* **1931**, *12*, 593−601.

(53) Wood, D. L.; Tauc, J. Weak Absorption Tails in Amorphous Semiconductors. *Phys. Rev. B: Condens. Matter Mater. Phys.* **1972**, *5*, 3144−3151.

(54) Ge, M.; Zhu, N.; Zhao, Y.; Li, J.; Liu, L. Sunlight-assisted Degradation of Dye Pollutants in Ag_3PO_4 Suspension. *Ind. Eng. Chem. Res.* **2012**, *51*, 5167−5173.

(55) Tang, C.; Liu, E.; Wan, J.; Hu, X.; Fan, J. Co_3O_4 Nanoparticles Decorated Ag_3PO_4 Tetrapods as an Efficient Visible-light-driven Heterojunction Photocatalyst. *Appl. Catal., B* **2016**, *181*, 707−715.

(56) Teoh, W. Y.; Scott, J. A.; Amal, R. Progress in Heterogeneous Photocatalysis: From Classical Radical Chemistry to Engineering Nanomaterials and Solar Reactors. *J. Phys. Chem. Lett.* **2012**, *3*, 629−639.

(57) Banerjee, S.; Pillai, S. C.; Falaras, P.; O'Shea, K. E.; Byrne, J. A.; Dionysiou, D. D. New Insights into the Mechanism of Visible Light Photocatalysis. *J. Phys. Chem. Lett.* **2014**, *5*, 2543−2554.

(58) Chen, L.; Yang, S.; Huang, Y.; Zhang, B.; Kang, F.; Ding, D.; Cai, T. Degradation of Antibiotics in Multi-component Systems With Novel Ternary $AgBr$/Ag_3PO_4@natural Hematite Heterojunction Photocatalyst under Simulated Solar Light. *J. Hazard. Mater.* **2019**, *371*, 566−575.

(59) Wang, F.; Feng, Y.; Chen, P.; Wang, Y.; Su, Y.; Zhang, Q.; Zeng, Y.; Xie, Z.; Liu, H.; Liu, Y.; Lv, W.; Liu, G. Photocatalytic Degradation of Fluoroquinolone Antibiotics using Ordered Mesoporous g-C_3N_4 under Simulated Sunlight Irradiation: Kinetics, Mechanism, and Antibacterial Activity Elimination. *Appl. Catal., B* **2018**, *227*, 114−122.

(60) Ahmadi, M.; Ramezani Motlagh, H.; Jaafarzadeh, N.; Mostoufi, A.; Saeedi, R.; Barzegar, G.; Jorfi, S. Enhanced Photocatalytic Degradation of Tetracycline and Real Pharmaceutical Wastewater using MWCNT/TiO_2 Nano-composite. *J. Environ. Manage.* **2017**, *186*, 55−63.

(61) Katsumata, H.; Taniguchi, M.; Kaneco, S.; Suzuki, T. Photocatalytic Degradation of Bisphenol A by Ag_3PO_4 under Visible Light. *Catal. Commun.* **2013**, *34*, 30−34.

(62) Global Action Plan on Antimicrobial Resistance. ⟨https://www.who.int/antimicrobial-resistance/global-action-plan/en/⟩ (accessed June 9, 2020).

(63) Vestergaard, M.; Frees, D.; Ingmer, H. Antibiotic Resistance and the MRSA Problem. *Microbiol. Spectrum* **2019**, *7* (2), 1−23.

(64) Macedo, N. G.; Machado, T. R.; Roca, R. A.; Assis, M.; Foggi, C. C.; Puerto-Belda, V.; Mínguez-Vega, G.; Rodrigues, A.; San-Miguel, M. A.; Cordoncillo, E.; Beltrán-Mir, H.; Andrés, J.; Longo, E. Tailoring the Bactericidal Activity of Ag Nanoparticles/α-Ag_2WO_4 Composite Induced by Electron Beam and Femtosecond Laser Irradiation: Integration of Experiment and Computational Modeling. *ACS Appl. Bio Mater.* **2019**, *2*, 824−837.

(65) Joya, Y. F.; Liu, Z.; Wang, T. Characterization and Antibacterial Functions of Ag−TiO_2 and W−TiO_2 Nanostructured thin Films Prepared by Sol-gel/Laser-induced Technique. *Appl. Phys. B* **2011**, *105*, 525−536.

(66) Jiang, X.; He, W.; Zhang, X.; Wu, Y.; Zhang, Q.; Cao, G.; Zhang, H.; Zheng, J.; Croley, T. R.; Yin, J.-J. Light-induced Assembly of Metal Nanoparticles on ZnO Enhances the Generation of Charge Carriers, Reactive Oxygen Species, and Antibacterial Activity. *J. Phys. Chem. C* **2018**, *122*, 29414−29425.

(67) Hong, Y.; Zeng, J.; Wang, X.; Drlica, K.; Zhao, X. Post-stress Bacterial Cell Death Mediated by Reactive Oxygen Species. *Proc. Natl. Acad. Sci. U.S.A.* **2019**, *116*, 10064−10071.

(68) Dovesi, R.; Orlando, R.; Erba, A.; Zicovich-Wilson, C. M.; Civalleri, B.; Casassa, S.; Maschio, L.; Ferrabone, M.; De La Pierre, M.; D'Arco, P.; Noël, Y.; Causà, M.; Rérat, M.; Kirtman, B. CRYSTAL14: A Program for the ab Initio Investigation of Crystalline Solids. *Int. J. Quantum Chem.* **2014**, *114*, 1287−1317.

(69) Dovesi, R.; Saunders, V. R.; Roetti, C.; Orlando, R.; Zicovich-Wilson, C. M.; Pascale, F.; Civalleri, B.; Doll, K.; Harrison, N. M.; Bush, I. J.; D'Arco, P.; Llunel, M.; Causà, M.; Noël, Y. *CRYSTAL14 User's Manual, Theoretical Chemistry Group*; University of Turin: Italy, 2014.

(70) Becke, A. D. Density-functional Thermochemistry. III. The Role of Exact Exchange. *J. Chem. Phys.* **1993**, *98*, 5648−5652.

(71) Lee, C.; Yang, W.; Parr, R. G. Development of the Colle-salvetti Correlation-energy Formula into a Functional of the Electron Density. *Phys. Rev. B: Condens. Matter Mater. Phys.* **1988**, *37*, 785−789.

(72) Crystal. ⟨http://www.crystal.unito.it/Basis_Sets/Ptable.html⟩ (accessed June 5, 2020).

(73) Hay, P. J.; Wadt, W. R. Ab Initio Effective Core Potentials for Molecular Calculations. Potentials for the Transition Metal Atoms Sc to Hg. *J. Chem. Phys.* **1985**, *82*, 270−283.

(74) de Foggi, C. C.; de Oliveira, R. C.; Fabbro, M. T.; Vergani, C. E.; Andres, J.; Longo, E.; Machado, A. L. Tuning the Morphological, Optical, and Antimicrobial Properties of α-Ag_2WO_4 Microcrystals Using Different Solvents. *Cryst. Growth Des.* **2017**, *17*, 6239−6246.

(75) CLSI. *Methods for Dilution Antimicrobial Susceptibility Tests for Bacteria that Grow Aerobically*; Clinical and Laboratory Standards Institute: Wayne, PA, 2006.

(76) Foggi, C. C.; Fabbro, M. T.; Santos, L. P. S.; de Santana, Y. V. B.; Vergani, C. E.; Machado, A. L.; Cordoncillo, E.; Andrés, J.; Longo, E. Synthesis and Evaluation of α-Ag_2WO_4 as Novel Antifungal Agent. *Chem. Phys. Lett.* **2017**, *674*, 125−129.